Chapter 4

An accurate method for computing the viscous, weakly compressible magnetic Rayleigh-Taylor instability in cylindrical geometry

4.1 Introduction

While the original Rayleigh-Taylor instability (RTI), pioneered by Lord Rayleigh in 1883 [50], and Sir G.I. Taylor in 1950 [59], considered horizontal planar flow, generalisations to this basic RTI problem have since been devised. The RTI in cylindrical coordinates was evidently first considered by Bell [8] in 1951.

Bell discovered that when considering curved geometry, additional effects can occur, which have no equivalent in the basic Cartesian geometry. In the linear model derived by Bell in cylindrical coordinates, the curvature of the interface contributes to the evolution of the interface in time. It is, in fact, possible for an otherwise stable system to in fact become unstable due to the curvature of the interface. In 1954, Plesset [49] derived the analogous result for spherical coordinates, and this effect is now collectively known as the Bell-Plesset effect. The combination of cylindrical coordinates together with magnetic effects first appeared in a study by Harris [28] in 1962.

As for the case of the MRTI in Cartesian geometry, study in the period from 1980 to the present in the case of cylindrical geometry has focussed primarily on numerical analysis of both the RTI and MRTI in the non-linear regime. A much smaller volume of work in this period considers the RTI in the linear regime. Papers by Mikaelian [43] and Yu & Livescu [63] in 2005 and 2008 respectively are two examples from the present era that consider linear effects of the RTI in cylindrical coordinates. Mikaelian considered the three dimensional RTI with mulitple interfaces where the fluids are arranged in a system of N cylindrical coaxial shells. In the case where $N = 3$, Mikaelian showed that, for high frequency perturbations, the system of differential equations decouples, so that Bell's equation can be applied at each interface independently for such a perturbation. Yu & Livescu defined a geometry parameter and considered how the qualitative nature of the flow changed as the flow varied from 2D axisymmetric (r, z) to 3D (r, θ, z) to 2D circular (r, θ) . Specifically, a comparison between two configurations is made. The convergent configuration is similar to the configuration of this thesis, whereby a heavy fluid surrounds a light fluid, and gravity is directed radially inwards. The divergent configuration is vice-versa, that is, a light fluid surrounds a heavy fluid, and gravity is directed radially outwards. The main result is that the growth rate of the interface in the convergent case is faster than for the divergent case, with the exception of the 2D circular regime, where the reverse occurs. For this reason, it is concluded

that the 3D results are qualitatively the same as for the 2D axisymmetric case, but qualitatively different to the 2D circular case.

The MRTI is the subject of frontier research in the field of astrophysics, with the study of HII regions and nebulae being the focus of applications in this chapter. These similar topics differ in that the ionization is higher in the case of nebulae compared with HII regions [53]. The basic theory behind the formation of such structures is well known, beginning with the classic 1939 Strömgren paper [58] in which the problem of the ionization and excitation of interstellar hydrogen was modelled by what is now known as a Strömgren sphere. Later, in 1954, Kahn considered in detail the acceleration of interstellar clouds by ionizing radiation [34]. The first to consider magnetic effects was Spitzer in 1956 [42], in which a lower limit to the mass that can be gravitationally bound was calculated. The basic theory of HII regions has been a textbook result from as early as 1978 with the subsequent work by Spitzer [53]. Modern numerical treatments consider the ideal MHD equations [26], and even photoionization and recombination in some cases [4, 27, 44]. The numerical component of such works is performed by various algorithms, such as Athena [56] in the case of [27], SPH/N [7] for works by Dale and Bonnell [17, 18] and the PHAB-C^2 code [30] used by Arthur et. al [4]. Mizuta found that when recombination is included, the growth rates were observed to be similar to the isothermal model of Williams [62].

The contents of this chapter contain a spectral-numerical method used to calculate the density, vorticity and current density of the fluid in cylindrical geometry. As for the model presented in chapter three, the methodology used in this current chapter is able to satisfy the condition requiring zero divergence of the magnetic field at all points in the space at all times in an exact, analytic fashion. The evolution of initially concentric fluids is shown to be highly dependant on a parameter called the magnetic Froude number, which represents a ratio of the strength of magnetic forces to gravitational forces. A variety of flow configurations is possible, with striking features of various simulated flows

compared with real flows as observed in HII regions and nebulae. The ability for the model of this chapter to predict a variety of such features in unstable flows gives some confidence as to the accuracy of the calculations.

4.2 Weakly Compressible, Viscous Model

This section presents a viscous model for the MRTI of two fluids arranged initially in two concentric discs, with the lighter fluid of density ρ_1 and magnetic permeability μ_1 interior to the heavier fluid of density ρ_2 and permeability μ_2. The initial interface of the two fluids is the circle located at radius $r = a$ from the origin, and the boundary of the computational domain is taken to be the circle $r = b$, for convenience. An opportune representation of the geometry is the cylindrical polar coordinate system (r, θ), which is defined from the rudimentary Cartesian (x, y) coordinate system by the conventional relations $x = r\cos\theta$ and $y = r\sin\theta$. We employ the Boussinesq approximation from Farrow and Hocking [23], replacing the two fluids of densities ρ_1 and ρ_2 with a single fluid of continuous density variation ρ. For this approximation to be valid, we require $\rho \approx \rho_1$ in the region $0 < r < a$ and $\rho \approx \rho_2$ in the region $a < r < b$. We also require that the change in ρ in the neighbourhood of $r = a$ is to be both rapid and smooth. The form of the density is thus $\rho = \rho_0 + \overline{\rho}$, where ρ_0 is a constant density component, and $\overline{\rho}$ is a small variable component. A gravitational field is directed radially inwards and is described by -g$\hat{\boldsymbol{e}}_{\boldsymbol{r}}$. Finally, we set $\mu_1 = \mu_2 = 1$ for simplicity, since $\mu \approx 1$ for many applications.

The governing equations of this model are a combination of Navier-Stokes' and Maxwell's equations. These equations take a similar form to the corresponding equations developed in the previous chapter. For convenience, we give a self contained development in this chapter due to a small number of differences. Under the Boussinesq approximation, the conventional equation representing the conservation of mass $\partial\rho/\partial t + \boldsymbol{\nabla}\cdot(\rho\boldsymbol{v}) = 0$ is split into the following two

equations,

$$\boldsymbol{\nabla} \cdot \boldsymbol{v} = 0, \tag{4.1}$$

$$\frac{\partial \overline{\rho}}{\partial t} + \boldsymbol{v} \cdot \boldsymbol{\nabla} \overline{\rho} = \epsilon_1 \boldsymbol{\nabla}^2 \overline{\rho}, \tag{4.2}$$

where the small Eckmann diffusion term on the right hand side of equation (4.2) has been added for the purpose of numerical stability. The conservation of momentum with both gravitational and Lorentz forces as well as viscous effects,

$$\frac{\partial (\rho \boldsymbol{v})}{\partial t} + (\boldsymbol{v} \cdot \boldsymbol{\nabla})(\rho \boldsymbol{v}) + \boldsymbol{\nabla}\left(p + \frac{B^2}{2\mu}\right) = -\rho g \hat{\boldsymbol{e}}_{\boldsymbol{r}} + \frac{1}{\mu}(\boldsymbol{B} \cdot \boldsymbol{\nabla})\boldsymbol{B} + \rho \nu \boldsymbol{\nabla}^2 \boldsymbol{v},$$

simplifies somewhat under the Boussinesq approximation, since terms proportional to $\overline{\rho}$ are deemed to be negligible, with the exception of the gravity force term $-\rho g \hat{\boldsymbol{e}}_{\boldsymbol{r}}$. Under this regime, the conservation of momentum takes the form

$$\rho_0 \left[\frac{\partial \boldsymbol{v}}{\partial t} + (\boldsymbol{v} \cdot \boldsymbol{\nabla})\boldsymbol{v}\right] + \boldsymbol{\nabla} p^* = -\overline{\rho} g \hat{\boldsymbol{e}}_{\boldsymbol{r}} + \frac{1}{\mu}(\boldsymbol{B} \cdot \boldsymbol{\nabla})\boldsymbol{B} + \rho_0 \nu \boldsymbol{\nabla}^2 \boldsymbol{v}, \tag{4.3}$$

where $p^* = p + \rho_0 g r + B^2/(2\mu)$.

Next, the absence of magnetic monopoles requires

$$\boldsymbol{\nabla} \cdot \boldsymbol{B} = 0 \tag{4.4}$$

and, finally, Faraday's Law takes the form

$$\frac{\partial \boldsymbol{B}}{\partial t} = -\boldsymbol{\nabla} \times \boldsymbol{E}.$$

The electric field $\boldsymbol{E}$ in Faraday's Law can be eliminated by substitution of the Lorentz equation $\boldsymbol{J} = \sigma(\boldsymbol{E} + \boldsymbol{v} \times \boldsymbol{B})$ as well as Ampere's Law $\boldsymbol{\nabla} \times \boldsymbol{B} = \mu \boldsymbol{J}$ and making use of the vector identity $\boldsymbol{\nabla} \times (\boldsymbol{\nabla} \times \boldsymbol{B}) = \boldsymbol{\nabla}(\boldsymbol{\nabla} \cdot \boldsymbol{B}) - \boldsymbol{\nabla}^2 \boldsymbol{B}$ to obtain

$$\frac{\partial \boldsymbol{B}}{\partial t} = \boldsymbol{\nabla} \times (\boldsymbol{v} \times \boldsymbol{B}) + \frac{1}{\mu\sigma} \boldsymbol{\nabla}^2 \boldsymbol{B}. \tag{4.5}$$

We remark that thermal considerations have been ignored due to results by Crutcher [16] in which a study of the properties of 27 interstellar clouds showed that magnetic effects dominate thermal effects in such regions, as well as repeating the comment from the introduction in which Mizuta [44] found that when recombination is included, the growth rates were observed to be similar to the isothermal model of Williams [62].

At time $t = 0$, a fluid dipole of strength p_D located at the origin and directed along the x axis, and a magnetic dipole of strength q_D also located at the origin and directed along the x axis are switched on impulsively. At this instant, the flow is irrotational, and can be described by a fluid potential Φ and a magnetic potential $\mathcal{X}$, given by

$$\Phi = \frac{p_D \cos\theta}{2\pi r}; \quad \mathcal{X} = \frac{q_D \cos\theta}{2\pi r}. \tag{4.6}$$

Non-dimensional variables are now introduced; the scales for length and density are given naturally by the quantities a and ρ_0 respectively. One may use the fluid dipole strength p_D together with the length scale a to derive scales for both time, a^3/p_D, and speed, p_D/a^2. The scale for magnetic field strength unsurprisingly requires the quantity q_D, and is given by q_D/a^2. A reference pressure of $p_D^2\rho_0/a^4$ ensues. Several dimensionless parameters control the behaviour of the system. The density ratio $D = \rho_2/\rho_1$ is required to be greater than 1 for the case of interest in this thesis which is unstable growth, but close to 1 so that $D-1$ is small in order for the Boussinesq approximation to be valid. We define the fluid Froude number F and magnetic Froude number G to be

$$F^2 = \frac{p_D^2}{ga^5}; \quad G^2 = \frac{q_D^2}{\rho_0 \mu g a^5}.$$

The parameter F is essentially a ratio of inertia to gravitational forces, while G represents the relative strength of magnetic and gravitational forces. The fluid

Reynolds number R_e and the magnetic Reynolds number R_m, defined by

$$R_e = \frac{p_D}{\nu a}; \quad R_m = \frac{p_D \mu \sigma}{a},$$

are assumed to be large in this chapter, that is, inertia forces dominate shear forces and advection of the magnetic field $\boldsymbol{B}$ is far more significant than diffusion of $\boldsymbol{B}$. This is comparable with the models of other works that study HII regions, such as those by Fukuda & Hanawa [26] and Gendelev & Krumholz [27] in which the ideal MHD equations are used, that is $R_e \to \infty$ and $R_m \to \infty$. Finally, the dimensionless Eckmann diffusion coefficient takes the form $E = \epsilon_1 a / p_D$, and is considered to be very small in this chapter for the purpose of numerical stability.

For time $t > 0$, the flow will become rotational in nature, hence the use of the potential functions (4.6) is not appropriate. However, under the Boussinesq approximation, there is still an incompressible component to the velocity $\boldsymbol{v}$ in view of equation (4.1). In the magnetic case, the absence of monopoles guarantees that $\boldsymbol{B}$ is incompressible, regardless of any approximation. We use a stream function approach to satisfy these two relations exactly. It is convenient to replace the conventional radial and azimuthal velocity components (u, v) with the modified components $\left(\tilde{U}, v\right)$, where $\tilde{U} = ru$. In these variables, we write the modified velocity components in terms of the fluid stream function Ψ as

$$\tilde{U} = \frac{\partial \Psi}{\partial \theta}; \quad v = -\frac{\partial \Psi}{\partial r} \tag{4.7}$$

A similar argument results in the modified magnetic field components being written in terms of the magnetic stream function $\mathcal{X}$ as

$$\tilde{B_r} = \frac{\partial \mathcal{X}}{\partial \theta}; \quad B_\theta = -\frac{\partial \mathcal{X}}{\partial r}, \tag{4.8}$$

where $\tilde{B_r} = rB_r$. Conjoint with each stream function is an associated vorticity

function, and we define

$$\xi = -\nabla^2\Psi; \quad \Upsilon = -\nabla^2\mathcal{X}$$

to be the fluid and magnetic vorticity functions respectively. The scalar functions ξ and Υ are the $\hat{\boldsymbol{e}}_{\boldsymbol{z}}$ components of the corresponding vectors $\boldsymbol{\nabla} \times \boldsymbol{v}$ and $\boldsymbol{\nabla} \times \boldsymbol{B}$, and represent twice the angular speed and twice the magnetic field magnitude in each case. It is also convenient to define a modified density function by $\tilde{R} = \overline{\rho}/r$, similar to Forbes [25]. In view of the stream function formulation, the entire system of equations is reduced to the following three transport equations for density, vorticity and magnetic vorticity (current),

$$r\frac{\partial \tilde{R}}{\partial t} + \tilde{U}\left(\frac{\partial \tilde{R}}{\partial r} + \frac{R}{r}\right) + v\frac{\partial \tilde{R}}{\partial \theta} = E\left(\nabla^2\tilde{R} + 2\frac{\partial \tilde{R}}{\partial r} + \frac{\tilde{R}}{r}\right) \quad (4.9)$$

$$\frac{\partial \xi}{\partial t} + \frac{\tilde{U}}{r}\frac{\partial \xi}{\partial r} + \frac{v}{r}\frac{\partial \xi}{\partial \theta} - \frac{G^2}{F^2}\left(\frac{\tilde{B}_r}{r}\frac{\partial \Upsilon}{\partial r} + \frac{B_\theta}{r}\frac{\partial \Upsilon}{\partial \theta}\right) = \frac{1}{F^2}\frac{\partial \tilde{R}}{\partial \theta} + \frac{1}{R_e}\nabla^2\xi \quad (4.10)$$

$$G^2\frac{\partial \Upsilon}{\partial t} = G^2\nabla^2 L + \frac{G^2}{R_m}\nabla^2\Upsilon \quad (4.11)$$

where $L = (\boldsymbol{v} \times \boldsymbol{B}) \cdot \hat{\boldsymbol{e}}_{\boldsymbol{z}}$.

We now seek a spectral solution to the non-linear system of equations (4.9)-(4.11) that satisfies given boundary and initial conditions exactly. This chapter imposes the condition that as $r \to 0$, the flow converges to the irrotational solution (4.6), that is,

$$\begin{aligned}
&\tilde{U} \to -\frac{\cos\theta}{2\pi r}; \quad v \to -\frac{\sin\theta}{2\pi r^2}; \quad \Psi \to -\frac{\sin\theta}{2\pi r}; \quad \xi \to 0 \\
&\tilde{B}_r \to -\frac{\cos\theta}{2\pi r}; \quad B_\theta \to -\frac{\sin\theta}{2\pi r^2}; \quad \mathcal{X} \to -\frac{\sin\theta}{\in\pi\nabla}; \quad \mp \to \prime \\
&\tilde{R} \to 0; \quad \frac{\partial \tilde{R}}{\partial \theta} \to 0.
\end{aligned} \quad (4.12)$$

These conditions (4.12) represent the exact singular behaviour near the line dipoles. Along the outer dimensionless boundary $r = \beta = b/a$, convenient

conditions are given by

$$\begin{aligned}
&\tilde{U} = -\frac{\cos\theta}{2\pi\beta}; \quad v = -\frac{\sin\theta}{2\pi\beta^2}; \quad \Psi = -\frac{\sin\theta}{2\pi\beta}; \quad \xi = 0 \\
&\tilde{B}_r = -\frac{\cos\theta}{2\pi\beta}; \quad B_\theta = -\frac{\sin\theta}{2\pi\beta^2}; \quad \mathcal{X} = -\frac{\sin\theta}{\in\pi\beta}; \quad \mp = \prime \\
&\tilde{R} = \frac{D-1}{\beta}.
\end{aligned} \tag{4.13}$$

The initial condition for the density perturbation needs to correspond to an effective interface at $r = 1$. For this reason, we impose

$$\tilde{R}\left(r,\theta,0\right) = \begin{cases} 0 & ,0 < r < 1 \\ (D-1)/r & ,1 < r < \beta \end{cases} \tag{4.14}$$

for the density function $\tilde{R}\left(r,\theta,t\right)$. In addition to the fluid and magnetic dipoles that are switched on impulsively at time $t = 0$, we include a small impulsive sinusoidal disturbance of magnitude ϵ to the K-th Fourier mode of the stream functions, which results in the initial conditions

$$\Psi\left(r,\theta,0\right) = \mathcal{X}\left(\nabla,\theta,\prime\right) = -\frac{\sin\theta}{\in\pi\nabla} + \begin{cases} \epsilon r^K \sin\left(K\theta\right) & ,0 < r < 1 \\ \epsilon r^{-K} \sin\left(K\theta\right) & ,1 < r < \beta. \end{cases} \tag{4.15}$$

We are now ready for the full time dependent spectral representation of the quantities Ψ, $\mathcal{X}$ and $\tilde{R}$. The stream functions take a similar form,

$$\Psi\left(r,\theta,t\right) = -\frac{\sin\theta}{2\pi r} + \sum_{m=1}^{M}\sum_{n=1}^{N} A_{mn}\left(t\right) J_{2m}\left(\frac{j_{2m,n}}{\beta}r\right)\sin\left(2m\theta\right) \tag{4.16}$$

$$\mathcal{X}\left(\nabla,\theta,\sqcup\right) = -\frac{\sin\theta}{2\pi r} + \sum_{m=1}^{M}\sum_{n=1}^{N} D_{mn}\left(t\right) J_{2m}\left(\frac{j_{2m,n}}{\beta}r\right)\sin\left(2m\theta\right) \tag{4.17}$$

where the notation $J_\nu\left(z\right)$ denotes the ν-th order Bessel function of the first kind, and $j_{\nu,n}$ denotes the n-th zero of $J_\nu\left(z\right)$. One may obtain the spectral forms of both the velocity and magnetic field strength components by performing the appropriate differentiation given in equations (4.7) and (4.8) respectively. Only

even order trigonometric terms are included in the double series term, due to the interest in bipolar solutions in this section.

The spectral form of the density function is chosen with the auxiliary constraint that certain integrals with respect to variable r in equations (4.19)-(4.22) are required to be non singular in the limit that $r \to 0$, in the spectral method described below. We therefore represent the density by

$$\begin{aligned}\tilde{R}(r,\theta,t) =& \frac{(D-1)\,r^2}{\beta^3} + \sum_{n=1}^{N} C_n(t) \sin\left(\frac{n\pi r^2}{\beta^2}\right) \\ &+ \sum_{m=1}^{M}\sum_{n=1}^{N} B_{mn}(t)\, J_{2m}\left(\frac{j_{2m,n}}{\beta} r\right) \cos(2m\theta)\,. \end{aligned} \tag{4.18}$$

It is a trivial matter to see that the conditions (4.12) and (4.13) are satisfied exactly by the given representations (4.16) - (4.18). The ability to deal exactly with the singular behaviour of the line dipoles is a strength of the present spectral approach. The use of the sine function in the single summation term in the density representation is particularly convenient, allowing a greater portion of the upcoming decomposition to be performed analytically rather than numerically, compared with various other choices for this representation. To decompose the vorticity equation (4.10), we multiply it by the basis functions $rJ_{2k}(j_{2k,l}r/\beta)\sin(2k\theta)$ and integrate over the cylindrical region $0 < r < \beta, -\pi < \theta < \pi$. This is then simplified considerably, primarily by application of the rudimentary trigonometric orthogonality relations [1, p.77,78], as well as the following orthogonality relation of the Bessel functions,

$$\int_0^{\beta} rJ_{\nu}(j_{\nu,n}r/\beta)\, J_{\nu}(j_{\nu,l}r/\beta) = \begin{cases} 0, & n \neq l \\ \beta^2 J_{\nu+1}^2(j_{\nu,l})/2, & n = l \end{cases}$$

which has been scaled appropriately for this problem from the standard form found in [1, p.485]. After a little algebra, the following system of ordinary

differential equations (ODEs) for the coefficients A_{kl} ensues:

$$\frac{dA_{kl}}{dt} = -\frac{2}{\pi\left[j_{2k,l}J_{2k+1}\left(j_{2k,l}\right)\right]^2}\int_{-\pi}^{\pi}\int_{0}^{\beta}\left[\tilde{U}\frac{\partial\xi}{\partial r}+v\frac{\partial\xi}{\partial\theta}-\frac{G^2}{F^2}\left(\tilde{B}_r\frac{\partial\Upsilon}{\partial r}+B_\theta\frac{\partial\Upsilon}{\partial\theta}\right)\right]\times$$
$$J_{2k}\left(\frac{j_{2k,l}}{\beta}r\right)\sin\left(2k\theta\right)drd\theta-2k\left(\frac{\beta}{Fj_{2k,l}}\right)^2B_{kl}\left(t\right)-\frac{1}{R_e}\left(\frac{j_{2k,l}}{\beta}\right)^2A_{kl}\left(t\right). \tag{4.19}$$

The current equation (4.11) is decomposed in an identical fashion as for the vorticity equation, resulting in the following system of ODEs for the coefficients D_{kl}:

$$\frac{dD_{kl}}{dt} = -\frac{2}{\pi\left[j_{2k,l}J_{2k+1}\left(j_{2k,l}\right)\right]^2}\int_{-\pi}^{\pi}\int_{0}^{\beta}\mathcal{G}\left(r,\theta,t\right)rJ_{2k}\left(\frac{j_{2k,l}}{\beta}r\right)\sin\left(2k\theta\right)drd\theta$$
$$-\frac{1}{R_m}\left(\frac{j_{2k,l}}{\beta}\right)^2A_{kl}\left(t\right), \tag{4.20}$$

where the intermediate function

$$\begin{aligned}\mathcal{G}\left(r,\theta,t\right) =& U\nabla^2B_\theta+2\left(\left[\frac{\partial U}{\partial r}-\frac{U}{r}\right]\frac{\partial B_\theta}{\partial r}+\frac{1}{r^2}\frac{\partial U}{\partial\theta}\frac{\partial B_\theta}{\partial\theta}\right)\\ &+B_\theta\left(\nabla^2U-\frac{2}{r}\frac{\partial U}{\partial r}+\frac{2U}{r^2}\right)-v\left(\nabla^2\tilde{B}_r-\frac{2}{r}\frac{\partial\tilde{B}_r}{\partial r}+\frac{2\tilde{B}_r}{r^2}\right)\\ &-2\left(\left[\frac{\partial\tilde{B}_r}{\partial r}-\frac{\tilde{B}_r}{r}\right]\frac{\partial v}{\partial r}+\frac{1}{r^2}\frac{\partial v}{\partial\theta}\frac{\partial\tilde{B}_r}{\partial\theta}\right)-\tilde{B}_r\nabla^2v\end{aligned}$$

has been defined for convenience. We now consider the density equation (4.9) in order to obtain the ODEs for the coefficients B_{kl} and C_l. Firstly, the B_{kl} are obtained by multiplying equation (4.9) by basis functions $J_{2k}\left(j_{2k,l}r/\beta\right)\cos\left(2k\theta\right)$ and integrating over the cylindrical region $0<r<\beta, -\pi<\theta<\pi$. Again, orthogonality conditions are used to simplify the expression, resulting in a system

of ODEs for the B_{kl} in the form

$$\frac{dB_{kl}}{dt} = -\frac{2}{\pi\left[\beta J_{2k+1}\left(j_{2k,l}\right)\right]^2}\int_{-\pi}^{\pi}\int_0^{\beta}\left[\tilde{U}\frac{\partial\tilde{R}}{\partial r}+v\frac{\partial\tilde{R}}{\partial\theta}+\frac{\tilde{U}\tilde{R}}{r}\right]\times$$
$$J_{2k}\left(\frac{j_{2k,l}}{\beta}r\right)\cos\left(2k\theta\right)d\theta dr - E\left(\frac{j_{2k,l}}{\beta}\right)^2 B_{kl}\left(t\right)+\frac{2E}{\left[\beta J_{2k+1}\left(j_{2k,l}\right)\right]^2}\times$$
$$\sum_{n=1}^{N}B_{kn}\left(t\right)\int_0^{\beta}\left[2\left(\frac{j_{2k,n}}{\beta}\right)J_{2k}'\left(\frac{j_{2k,n}}{\beta}r\right)+\frac{1}{r}J_{2k}\left(\frac{j_{2k,n}}{\beta}r\right)\right]J_{2k}\left(\frac{j_{2k,l}}{\beta}r\right)dr. \tag{4.21}$$

To obtain the final system of ODEs for the C_n, we return to the density equation (4.9), but this time multiply by basis functions $\sin\left(l\pi r^2/\beta^2\right)$. The orthogonality relation,

$$\int_0^{\beta} r\sin\left(\frac{n\pi r^2}{\beta^2}\right)\sin\left(\frac{l\pi r^2}{\beta^2}\right)dr = \begin{cases}0, & n\neq l\\ \beta^2/4, & n=l\end{cases}$$

is used to simplify the expression, resulting in

$$\frac{dC_l}{dt} = -\frac{2}{\pi\beta^2}\int_{-\pi}^{\pi}\int_0^{\beta}\left(\tilde{U}\left[\frac{\partial\tilde{R}}{\partial r}+\frac{\tilde{R}}{r}\right]+v\frac{\partial\tilde{R}}{\partial\theta}\right)\sin\left(\frac{l\pi r^2}{\beta^2}\right)drd\theta$$
$$+E\left[\frac{36\left(D-1\right)}{\pi\beta^3 l}\right]\sin^2\left(\frac{l\pi}{2}\right)+\mathcal{F}\left(r\right), \tag{4.22}$$

where

$$\mathcal{F}\left(r\right) = \frac{32\pi}{\beta^4}\sum_{n=1}^{N}nC_n\left(t\right)\int_0^{\beta} r\cos\left(\frac{n\pi r^2}{\beta^2}\right)\sin\left(\frac{l\pi r^2}{\beta^2}\right)dr -$$
$$\frac{16\pi^2}{\beta^6}\sum_{n=1}^{N}n^2C_n\left(t\right)\int_0^{\beta} r^3\sin\left(\frac{n\pi r^2}{\beta^2}\right)\sin\left(\frac{l\pi r^2}{\beta^2}\right)dr +$$
$$\frac{4}{\beta^2}\sum_{n=1}^{N}C_n\left(t\right)\int_0^{\beta}\frac{1}{r}\sin\left(\frac{n\pi r^2}{\beta^2}\right)\sin\left(\frac{l\pi r^2}{\beta^2}\right)dr. \tag{4.23}$$

The integrals appearing in equation (4.23) can all be evaluated in closed form, making use of the cosine integral function [1, p.231],

$$Ci\left(z\right) = \gamma+\log z+\int_0^{z}\frac{\cos t-1}{t}\,dt,$$

in which $\gamma \approx 0.577$ is the Euler constant [1, p.255]. The equations (4.19) to (4.22) form a system of ODEs for the coefficients A_{kl} to D_{kl}. We invoke the classic fourth order Runge-Kutta method [5, p.371] to integrate the system forwards in time from an initial state at time $t = 0$. There is a small number of integrals that cannot be evaluated in closed form; these are calculated approximately by use of Gauss-Legendre quadrature in both the r and θ coordinates. The abscissae and weights for the Gauss-Legendre scheme are calculated by a MATLAB program written by von Winckel [61]. The initial conditions for the coefficients A_{kl} to D_{kl} are calculated by decomposition of equations (4.14) and (4.15). After simplification, including the use of various identities for the Bessel functions [1, p.361], one obtains in the case $K = 2$ (bipolar solutions),

$$\begin{aligned}
A_{1l}(0) =& \frac{2\epsilon}{J_3^2(j_{2,l})}\left[\frac{4}{(j_{2,l})^2}J_2\left(\frac{j_{2,l}}{\beta}\right) - \frac{J_1(j_{2,l})}{\beta^2 j_{2,l}}\right] \\
C_l(0) =& \frac{2(D-1)}{\beta}\left[\sqrt{\frac{2}{l}}\left\{S\left(\sqrt{2l}\right) - S\left(\sqrt{\frac{2l}{\beta}}\right)\right\} + \frac{\cos(l\pi)}{l\pi}\right] \\
D_{1l}(0) =& \frac{2\epsilon}{J_3^2(j_{2,l})}\left[\frac{4}{(j_{2,l})^2}J_2\left(\frac{j_{2,l}}{\beta}\right) - \frac{J_1(j_{2,l})}{\beta^2 j_{2,l}}\right]
\end{aligned} \tag{4.24}$$

where $S(z)$ is the Fresnel sine integral $\int_0^z \sin\left(\pi t^2/2\right) dt$ [1, p.300]. The initial value of those coefficients not listed above is zero.

4.3 Results

In this section, we present results of the spectral-numerical method of the previous section for a range of Magnetic Froude number values. This will enable the effect of a magnetic field on the growth of the MRTI to be observed. In order for the Boussinesq approximation to be valid, we require $D \approx 1$, and in view of this fact, we set the density ratio to $D = 1.05$. The initial disturbance mode is set to $K = 2$ since bipolar solutions are of primary interest in this chapter. A total of 31 Bessel modes, and thus 15 non-zero Fourier modes is found to be an appropriate balance between a representation that sufficiently spans the frequency domain, yet is numerically stable. For the latter consideration, it is known that the higher order modes are the most numerically unstable. The numerical value of both the fluid and magnetic Reynolds numbers is chosen to be 10^4; this results in inertia forces that are large in comparison with shear forces, and means that diffusion of the magnetic field is weak compared with advection. The reason that we consider such a low shear regime is in view of results by Zhang et al. [64] where it was shown that the RTI becomes more unstable in the high shear flow regime. With regards to the magnetic advection and diffusion, Chambers and Forbes [11] demonstrated that the RTI was largely unaffected by a magnetic field in the strong advection regime due to the weakness of induced currents, as discussed in chapter 3. This choice is comparable to other models in the literature that use the ideal MHD equations [26, 44, 27]. We also require the diffusion of the density function to be weak in some sense so that the single continuous, smooth fluid density function does indeed approximate the constant densities of the two fluid case. For this reason, a small diffusion coefficient of $\epsilon_1 = 10^{-4}$ is used. The outer numerical boundary is located at $\beta = 2$. This value is chosen in order for the observed features of the flow to be easily visible from the density plots, whilst being located far enough from the origin that it does not significantly affect the flow. The initial amplitude of the disturbance is set to $\epsilon = 0.03$. Finally, the fluid Froude number F takes

the value 2, since this is appropriate for a typical bipolar flow in astrophysics, as opposed to say a laboratory application whereby a light fluid is injected into a heavier one which requires $F \to \infty$. The numerical grid has a non-uniform spacing in both the r and θ coordinates due to the use of Gaussian quadrature. A total of 161 points in the r-coordinate over the range $0 < r < 2$ and 81 points in the θ-coordinate over the range $0 < \theta < \pi$ were used. Symmetry arguments were used to calculate the value of quantities in the range $-\pi < \theta < 0$. A time step of $1/200$ was found to give stable results in all cases. The accuracy of the numerical component of the method is deemed to be reliable by use of similar techniques as described in the results section of the previous chapter.

4.3.1 No magnetic field

We begin by considering the case in which there is no magnetic field. This is equivalent to setting the magnetic Froude number to $G = 0$ and all of the D_{kl} coefficients to 0. Figure 4.1 is a density plot that shows the configuration of the two fluids at the four times $t = 6, 9, 12$ and 15. The lighter of the two fluids is shown in purple (dark) with blue (soft) representing the heavier fluid. By time $t = 6$, the initially concentric configuration from time $t = 0$ has evolved into a dumbbell type shape for the lighter fluid. Motion of the lighter fluid in the x-direction is favoured over motion in the y-direction since the fluid dipole at the origin is oriented along the x-axis. This becomes even more apparent by the time $t = 15$. At this time, we also observe the classic mushroom roll-up of the interface for the two plumes. Much after this time, the single continuous, smooth density function fails to be able to distinguish between the heavy and light fluids near the interface due to diffusion and numerical error. These results are comparable with those of Forbes [25] in which a line source replaces the line dipole of this thesis. This comparison gives confidence in the method of this chapter, since a linearised solution is unavailable for comparison at early values of time. The main difference between the two configurations is that the lighter fluid penetrates further into the heavier fluid in the case of the line source, since

the effect of the line source is stronger than that of the line dipole for radius $r > 1$.

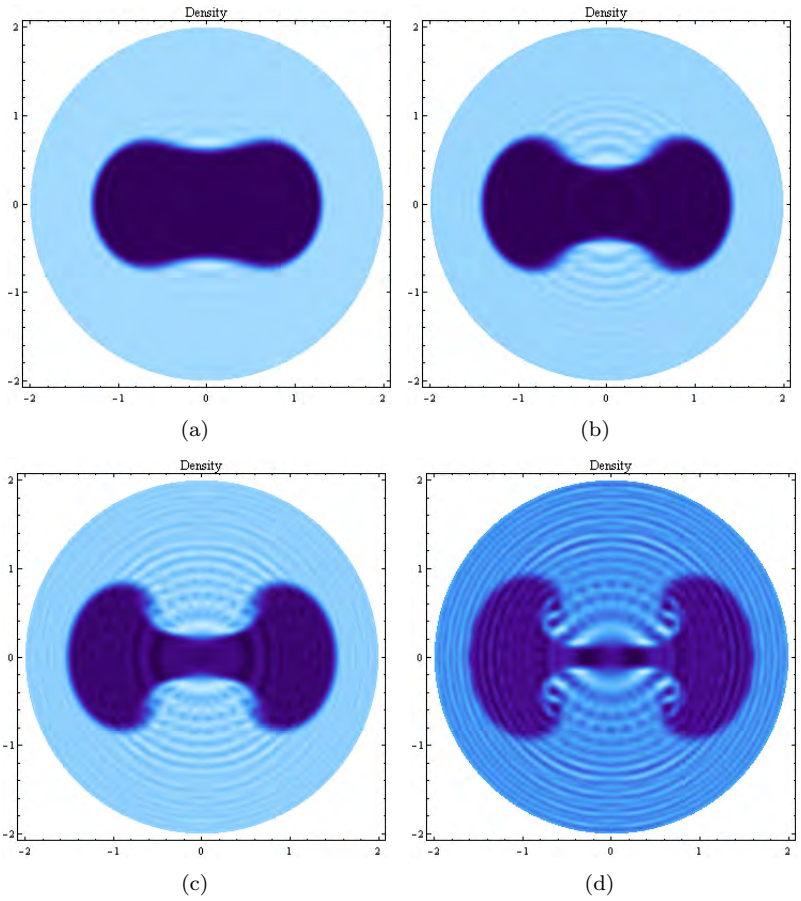

Figure 4.1: Density plot at the four times (a) $t = 6$, (b) $t = 9$, (c) $t = 12$ and (d) $t = 15$ in the absence of a magnetic field, showing the lighter fluid in purple (dark), and the heavier fluid in blue (soft). The magnetic Froude number is $G = 0$.

The results are also comparable with real physical observations such as those of HII regions and nebulae in the field of astrophysics. Figure 4.2 shows a rotated image of MyCn18, known more commonly as the hourglass nebula, taken by the Hubble Space Telescope in 1996 [52]. This nebula lies about 8000 light years from Earth in the southern constellation Musca. The three different colours in the image represent three different gases; nitrogen in red, hydrogen in green and oxygen in blue. Contemporary thinking is that the hourglass shape is produced

by the expansion of a fast stellar wind within a slowly expanding cloud which is denser near its equator than its poles [52]. The Rayleigh-Taylor instability is thus applicable to this situation. The fact that this configuration is reproduced with a magnetic Froude number of $G = 0$ gives rise to the possibility that the effects of gravitational forces completely dominate the effects of magnetic forces for this nebula. Verification of this is not directly possible due to very little information being available about this nebula. The hourglass shape of the nebula closely resembles the simulated density profile from figure 4.1(c).

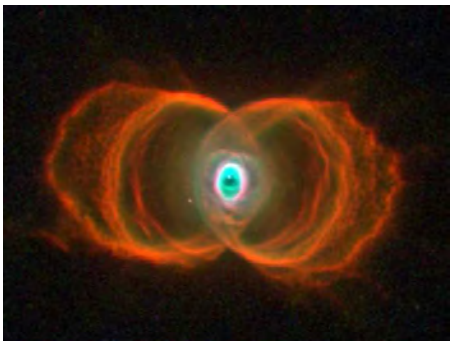

Figure 4.2: The "hourglass nebula", MyCn18, taken by the Hubble Space Telescope [52]. Credits: Raghvendra Sahai and John Trauger (JPL), the WFPC2 science team, and NASA.

When considering the vorticity of the fluids in the case of Cartesian geometry with a single mode disturbance, it is observed [24] that the vorticity is zero at almost all points in the fluid. There are just two small regions where the vorticity is non-zero; these positions are centred about the points where the curvature of the interface becomes infinite after a finite time in the non-viscous case. The case is very different in cylindrical geometry as there is non-zero vorticity at almost all points of the fluid. Notwithstanding this, it is observed that the magnitude of the vorticity is largest around the interface, but the more complicated distribution of vorticity compared with the case in Cartesian geometry makes vorticity a somewhat less useful quantity with which to explain the behaviour of the flow with time in the case of cylindrical geometry. We show how the vorticity evolves in figures 4.3. The same points in time are sampled as

for the case of the density above, so that it can be seen clearly that the vorticity is largest near the interface.

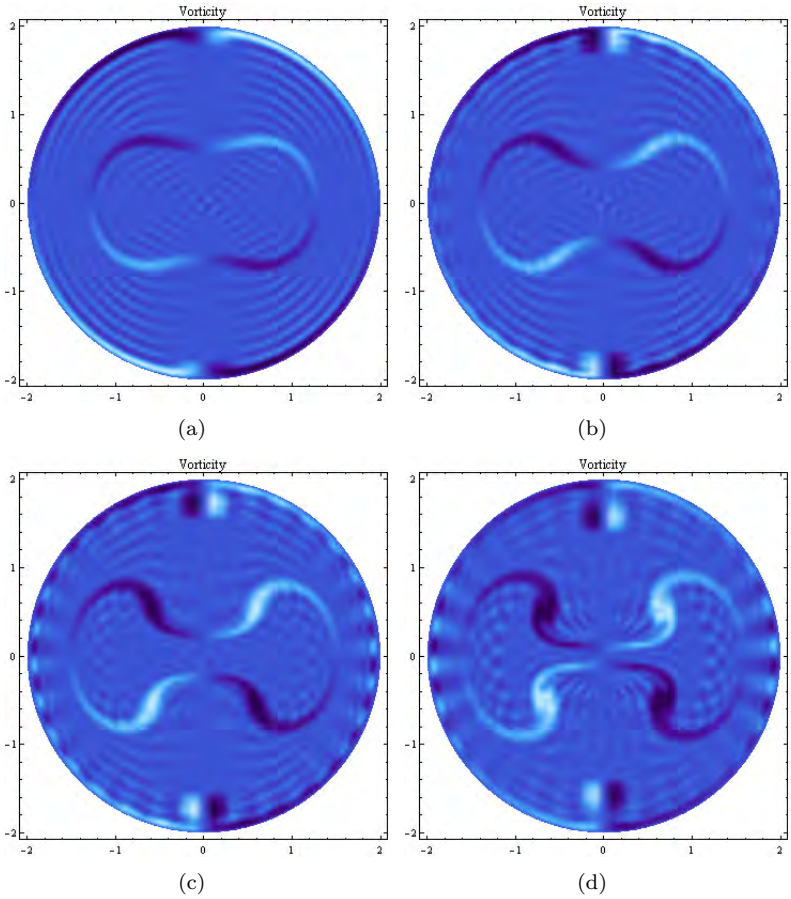

Figure 4.3: Vorticity plot at the four times (a) $t = 6$, (b) $t = 9$, (c) $t = 12$ and (d) $t = 15$, in the absence of a magnetic field, showing clockwise rotation in dark, and counter clockwise rotation in soft. The magnetic Froude number is $G = 0$.

4.3.2 Magnetic Field

The base magnetic field is due to the presence of a magnetic dipole located at the origin, directed along the x-axis. Of course, there is also an induced magnetic field due to the motion of the fluid across the magnetic field lines. The effect of the total magnetic field can be progressively made stronger by choosing larger values of the magnetic Froude number G. We begin with the case $G = 1$, in

which the magnetic effects are considered weaker than the fluid effects since the fluid Froude number is $F = 2$ and thus we have $G < F$. Figure 4.4 shows the configuration of the fluids at the same times as in the non-magnetic case so that we can see the effect that the presence of this field together with $G = 1$ has on the flow. At this value of G, the flow is qualitatively similar to the non-magnetic case, but suppressed in time. This is in agreement with Lenz' law, whereby the induced current flows in such a direction to oppose the change that caused it. The induced current flows when the fluid crosses the magnetic field lines; hence this motion and thus the growth of the instability is suppressed. We do not show contours of vorticity nor current density due to the reasons given in the previous case and in the interests of space.

The next consideration is the case where the fluid and magnetic effects may be considered to have equal weight due to the dimensionless Froude numbers taking the values $F = G = 2$. The flow configuration is shown in figures 4.5, again at identical times to the previous cases. In this regime, it is apparent that the presence of the magnetic field is not merely just suppressing the flow; the lighter fluid is penetrating deeper into certain regions of the heavier fluid compared with the non-magnetic case. This feature was not observed in Cartesian geometry, where the magnetic field acted only to suppress the flow. The configuration still features the classic mushroom shape of the previous cases, but the mushroom cap now appears thinner and more elongated.

This change is made even clearer by doubling the magnetic Froude number to $G = 4$. Figure 4.6 shows this case. The previous roundness of the mushroom cap now looks distorted, with the tips of the mushroom "snaking" into the lighter fluid. Even the stem of each mushroom is behaving differently now. Rather than a more-or-less uniform width stem, each stem appears more bulbous in regions near the origin, due to growth near the mushroom cap being suppressed.

We remark in particular on the likeness of the features from figure 4.6(c) and figure 4.7, which shows an image of NGC 6302 [45], otherwise known as the butterfly nebula. This picture was taken by the Hubble Space Telescope in

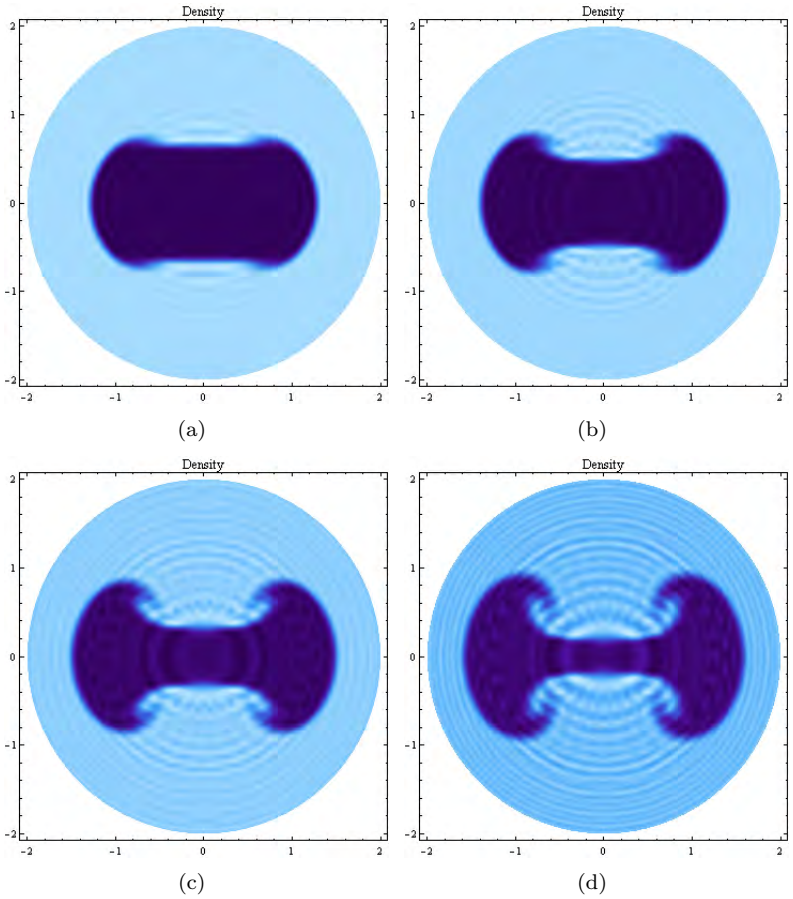

Figure 4.4: Density plot at the four times (a) $t = 6$, (b) $t = 9$, (c) $t = 12$ and (d) $t = 15$ in the absence of a magnetic field, showing the lighter fluid in purple (dark), and the heavier fluid in blue (soft). The magnetic Froude number is $G = 1$.

2009 in ultra-violet and visible light. This nebula is located in the constellation Scorpius, about 3800 light years from Earth within the Milky Way galaxy. The primary features of the nebula are the butterfly wings and the numerous finger like projections. Both the butterfly wings and finger projections are also present in the results of the numerical simulation shown in figure 4.6(c), which under rotation is of a similar form to the image of the butterfly nebula 4.7.

Finally, we re-double the magnetic Froude number to $G = 8$. In this regime, magnetic effects are very dominant over the fluid effects on the flow. The configurations given for this case in figure 4.8 are qualitatively very different to the

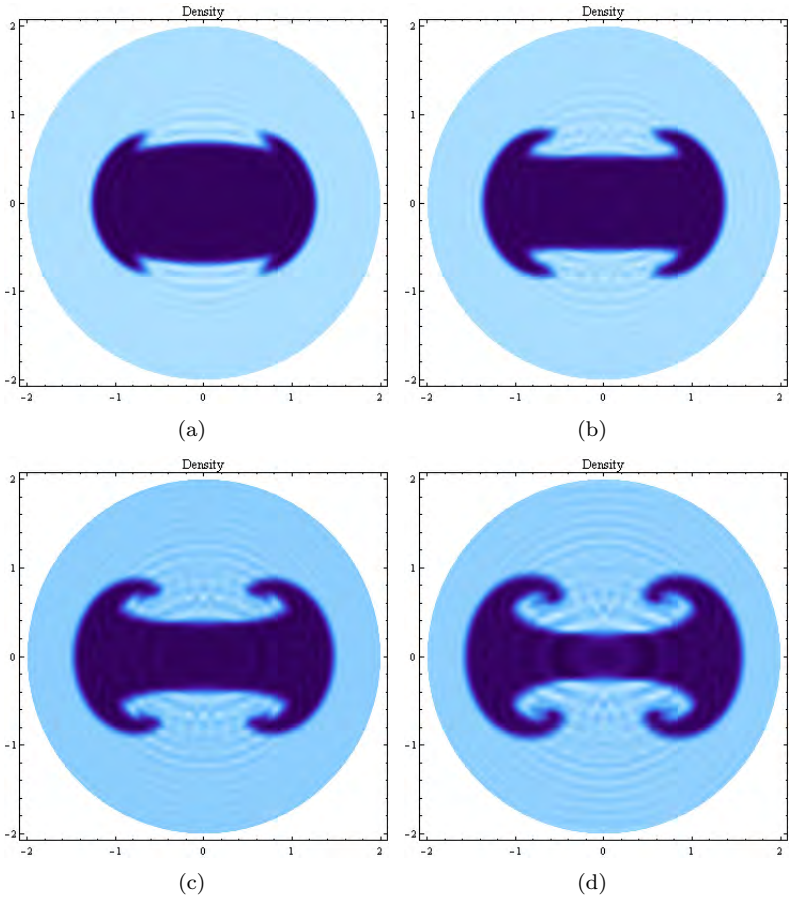

Figure 4.5: Density plot at the four times (a) $t = 6$, (b) $t = 9$, (c) $t = 12$ and (d) $t = 15$ in the absence of a magnetic field, showing the lighter fluid in purple (dark), and the heavier fluid in blue (soft). The magnetic Froude number is $G = 2$.

configurations that resulted from much lower magnetic Froude numbers. This is contrast to the case of Cartesian geometry, where it was observed [11] that the presence of a magnetic field merely suppressed the flow in time; it did not alter the regions that the lighter fluid could penetrate.

The "snaking" or "tentacular" nature of the flow from figure 4.8 is reminiscent of behaviour observed in the tarantula nebula, an image of which is available from either of the public websites [21, 22]. Unfortunately, due to copyright restrictions, this image can not be printed in this paper. The curled over light blue tentacle featured in the top right of the nebula image is especially

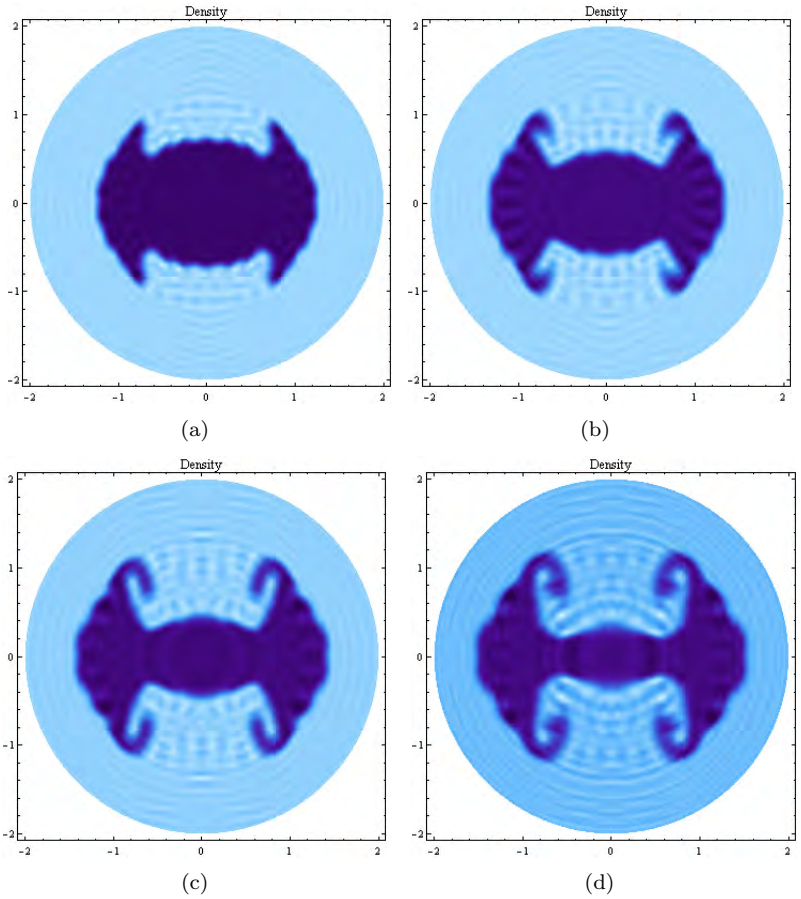

Figure 4.6: Density plot at the four times (a) $t = 6$, (b) $t = 9$, (c) $t = 12$ and (d) $t = 15$ in the absence of a magnetic field, showing the lighter fluid in purple (dark), and the heavier fluid in blue (soft). The magnetic Froude number is $G = 4$.

striking in similarity to the same region in the simulated image. This nebula is also known as the 30 Doradus nebula in the NGC 2070 star cluster. This cluster is one of the largest known star formation regions [22]. It is very bright, in fact bright enough to be observed optically despite it being located outside our Milky Way galaxy in the large Magellanic Cloud [3].

The effect of the polarity of the magnetic dipole was also considered, but was found to have no effect on the flow. In the interests of space, the results are thus not presented here. This result was as expected, since an earlier analysis of similar nature performed in Cartesian geometry [11] produced the same result.

Figure 4.7: The Butterfly nebula. Credit: NASA, ESA and The Hubble SM4 ERO Team [45].

This can be explained with the already mentioned Lenz' law argument as in chapter 3. The induced current always flows in the direction so as to oppose the change that caused it, hence the growth of the MRTI is suppressed by the same amount regardless of the polarity of the magnetic dipole located at the origin.

4.3.3 Higher mode disturbances

In this section, we present some results in which tripolar plumes evolve. The initial disturbance to generate such a configuration requires $K = 3$ in equation (4.15). This alteration to the quantity K in turn affects the spectral representations for both the streamfunctions and the density given previously by equations (4.16) and (4.18). In the present case of tripolar plumes, only the coefficients of trigonometric terms of an order that is a multiple of three are non-zero, and hence we may write the spectral forms of the streamfunctions as

$$\begin{aligned}\Psi(r,\theta,t) &= -\frac{\sin\theta}{2\pi r} + \sum_{m=1}^{M}\sum_{n=1}^{N} A_{mn}(t)\, J_{3m}\left(\frac{j_{3m,n}}{b}r\right)\sin(3m\theta) \\ \mathcal{X}(\nabla,\theta,\sqcup) &= -\frac{\sin\theta}{2\pi r} + \sum_{m=1}^{M}\sum_{n=1}^{N} D_{mn}(t)\, J_{3m}\left(\frac{j_{3m,n}}{b}r\right)\sin(3m\theta) \qquad (4.25)\end{aligned}$$

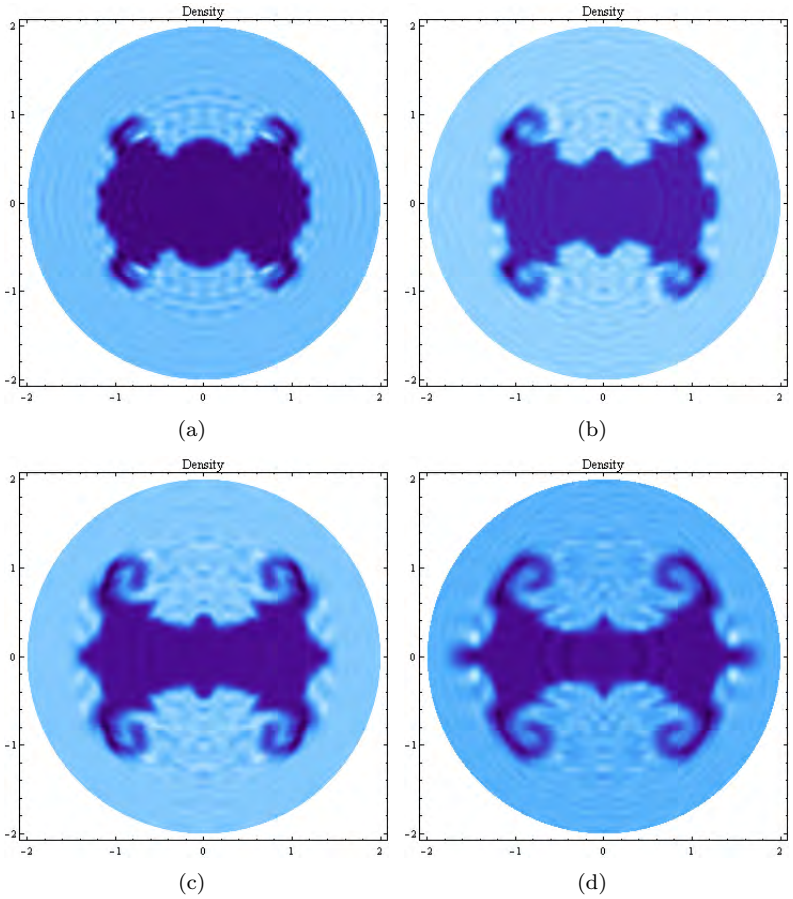

Figure 4.8: Density plot at the four times (a) $t = 6$, (b) $t = 9$, (c) $t = 12$ and (d) $t = 15$ in the absence of a magnetic field, showing the lighter fluid in purple (dark), and the heavier fluid in blue (soft). The magnetic Froude number is $G = 8$.

and the spectral form of the density function as

$$\tilde{R}(r,\theta,t) = \frac{(D-1)\,r^2}{b^3} + \sum_{n=1}^{N} C_n(t) \sin\left(\frac{n\pi r^2}{b^2}\right) + \sum_{m=1}^{M}\sum_{n=1}^{N} B_{mn}(t)\, J_{3m}\left(\frac{j_{3m,n}}{b} r\right) \cos(3m\theta)\,. \tag{4.26}$$

Whilst the main applications in the field of astrophysics require bipolar solutions, the study of the general case is valuable for a deeper understanding of the instability. A study by Matsuoka and Nishihara [40] on the topic of the associated RMI presents results depicting single, bipolar, tripolar and octopolar

plumes. The growth rates of bubbles (where light fluid penetrates a heavy fluid) and spikes (where heavy fluid penetrates a light fluid) are quantities of interest in the study of the RMI. A later paper by the same authors [39] argues that the results in which the disturbing mode is greater than or equal to three are fundamentally different to the case in the disturbing mode is less than three. Under the parameters used by the authors in that paper, the curvature of the spikes is positive for modes less than three, but negative for modes greater than three.

We now present a series of density plots showing the configuration of the two fluids at different points in time for a range of magnetic Froude numbers. The first case considers a magnetic Froude number of $G = 0$, which corresponds with the case of the non-magnetic RTI, in figure 4.9. The format of the figures from the previous section is retained, that is, the lighter of the two fluids is shown in purple (dark) with blue (soft) representing the heavier fluid. In order to facilitate a meaningful comparison, the same instants in time are sampled as for previous cases.

A comparison of figures 4.9 with figures 4.1 from section 4.3.1 shows that there is a greater degree of roll up in the case of the tripolar plume than for the bipolar plume under the same parameters. Matsuoka and Nishihara [40] argue that, due to the existence of two independent spatial scales when using cylindrical geometry, radius and wavelength, the growth rate is highly dependent on mode number. This same argument is used by the author of this thesis to justify the higher degree of roll up just observed in view of the fact that both radius and wavelength are used as spatial scales in the model of this chapter.

As was the case of the previous section, we alter the magnetic Froude number, and examine the effect of a magnetic field on the instability. The first case to include magnetism for the mode three disturbance has a magnetic Froude number of $G = 1$, and results for this case are shown in figure 4.10. In the case of the mode two disturbance, the classic mushroom cap shapes of the non-magnetic case gradually became more distorted as the magnetic Froude number

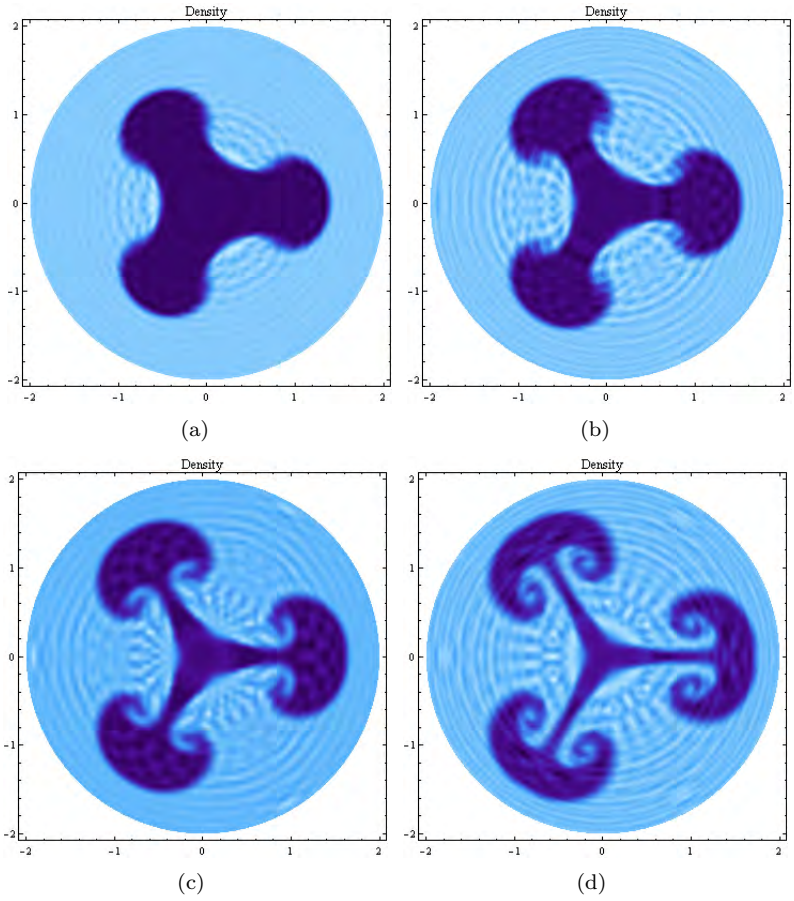

Figure 4.9: Density plot at the four times (a) $t = 6$, (b) $t = 9$, (c) $t = 12$ and (d) $t = 15$ in the absence of a magnetic field, showing the lighter fluid in purple (dark), and the heavier fluid in blue (soft). The magnetic Froude number is $G = 0$ and the disturbance mode is $K = 3$.

increased. The tips of the caps were seen as snakes of heavy fluid penetrating the light fluid. The same scenario is observed in the case of mode three disturbances, albeit at seemingly faster growth rates due to the fact that the time scale is dependent on the wave number. These snake like structures are clearly visible in the case of $G = 2$, in figure 4.11, with longer snakes appearing in the cases of magnetic Froude number $G = 4$ and $G = 8$ shown in figures 4.12 and 4.13.

As a further extension, we present a comparison of a configuration that evolves into five plumes with a famous nebula called the Rosette nebula. This

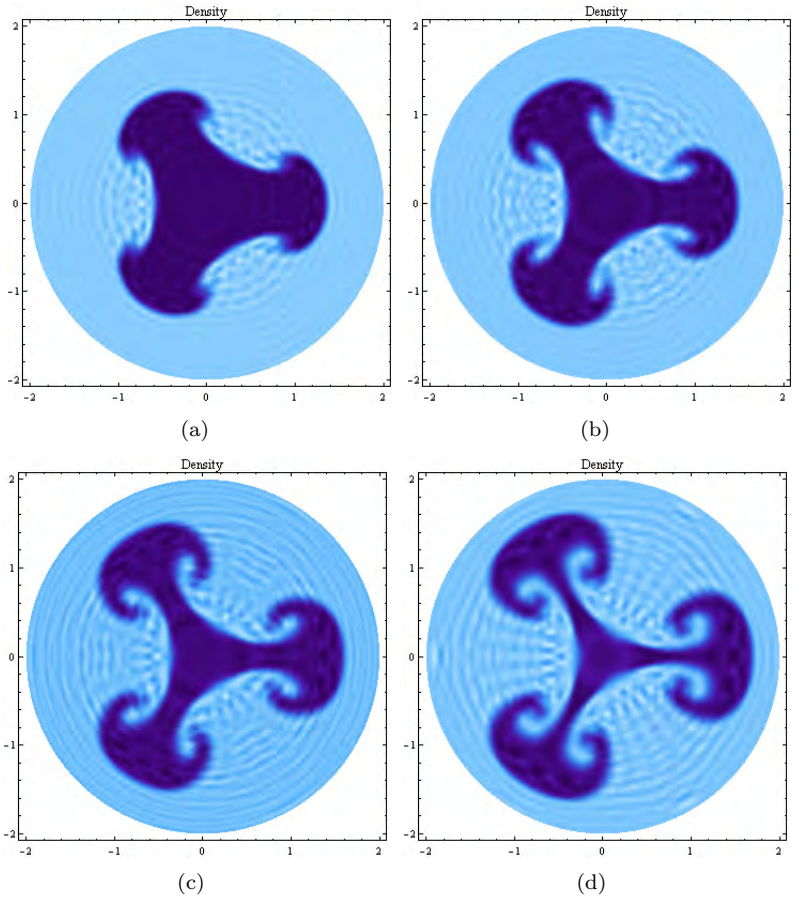

Figure 4.10: Density plot at the four times (a) $t = 6$, (b) $t = 9$, (c) $t = 12$ and (d) $t = 15$ in the absence of a magnetic field, showing the lighter fluid in purple (dark), and the heavier fluid in blue (soft). The magnetic Froude number is $G = 1$ and the disturbance mode is $K = 3$.

result requires an initial disturbance wave number of $K = 5$ in equation (4.15). The Rosette nebula, or NGC 2237 as it is more formally known, is a well studied HII region generated by a compact group of five stars. It is located at a distance of about 5000 light years from the Earth, in the Monoceros region inside the Milky Way band [54]. Figure 4.14(a) shows an image of the Rosette nebula [46] and figure 4.14(b) is the result of a numerical simulation using the method of this chapter. The main feature of the Rosette nebula is the five petal structure, which is able to be reproduced using the techniques of this chapter.

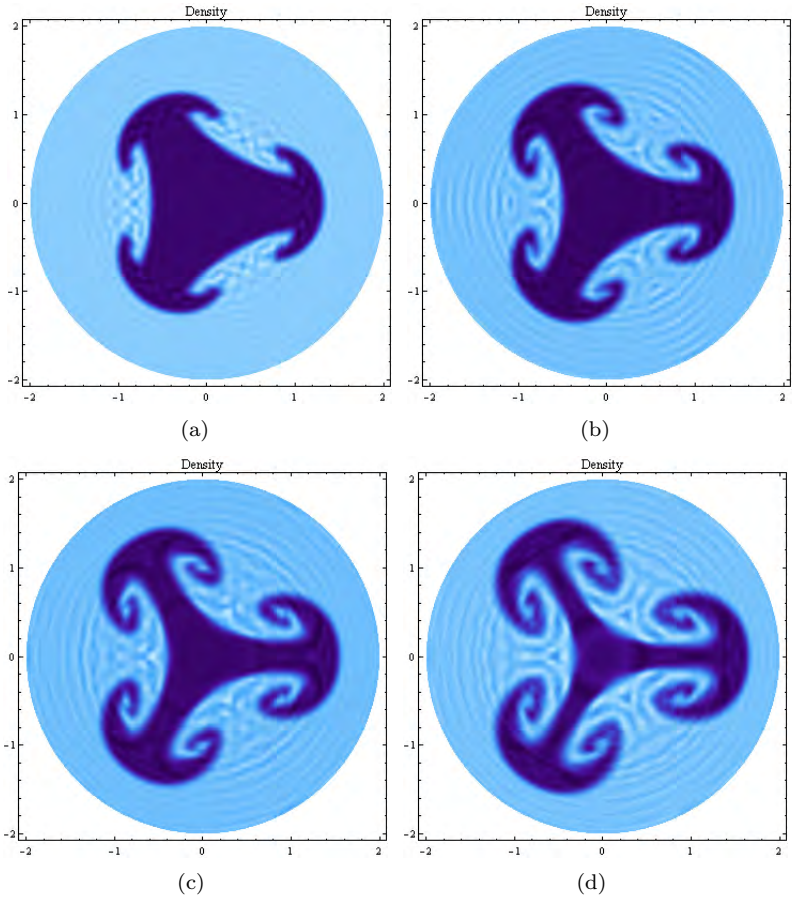

Figure 4.11: Density plot at the four times (a) $t = 6$, (b) $t = 9$, (c) $t = 12$ and (d) $t = 15$ in the absence of a magnetic field, showing the lighter fluid in purple (dark), and the heavier fluid in blue (soft). The magnetic Froude number is $G = 2$ and the disturbance mode is $K = 3$.

4.4 Conclusion

A spectral-numerical analysis of the MRTI has been performed to study the effect of a magnetic field on the RTI in cylindrical coordinates for viscous, weakly compressible flow. The mechanism for instability in cylindrical geometry is quite different from that in Cartesian geometry, due to the Bell-Plesset effect [49]. A key feature of the method from the current chapter was the use of a magnetic stream function which enabled the divergence-free nature of the magnetic field to be satisfied identically. This rules out the possibility that the results of this chapter are due to either fictitious magnetic monopoles or possible errors con-

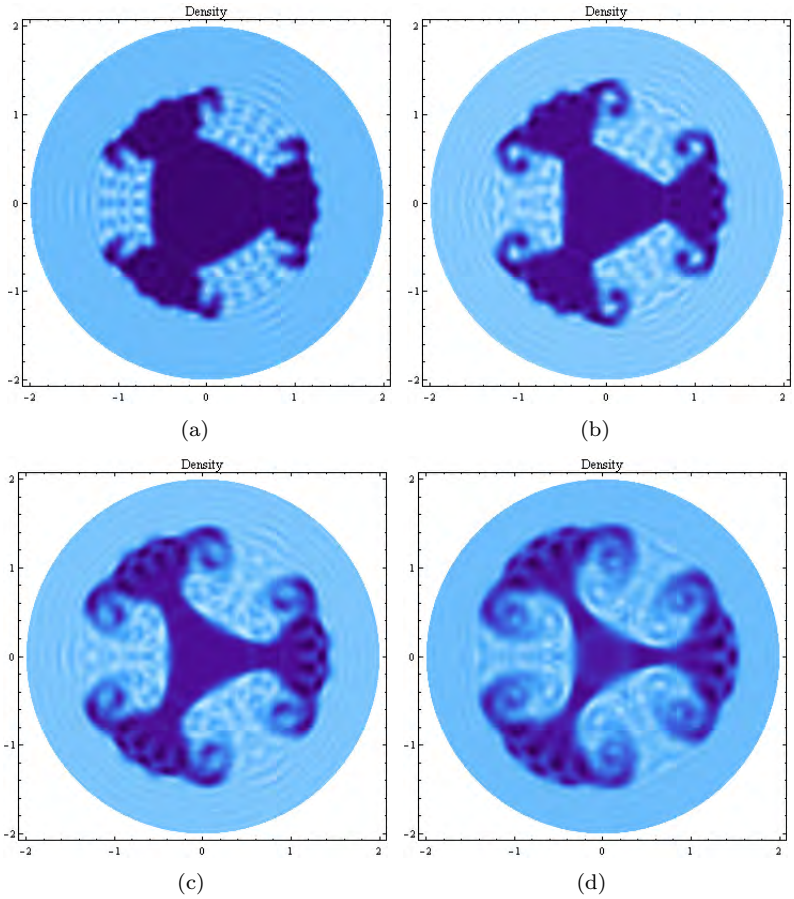

Figure 4.12: Density plot at the four times (a) $t = 6$, (b) $t = 9$, (c) $t = 12$ and (d) $t = 15$ in the absence of a magnetic field, showing the lighter fluid in purple (dark), and the heavier fluid in blue (soft). The magnetic Froude number is $G = 4$ and the disturbance mode is $K = 3$.

sequent of other assumptions, for example those used in constrained transport methods typical of the numerical schemes mentioned in the introduction. The presence of numerically generated magnetic monopoles was shown by Brackbill and Barnes [9] to produce a fictitious force parallel to the magnetic field, while the constrained transport methods require an artificial alteration of the magnetic field in order for it to remain divergence free at each time step.

By varying the magnetic Froude number it is possible to observe the effect that a base magnetic field due to a line dipole located at the origin and directed along the x-axis has on the flow. A qualitative change in the nature of the

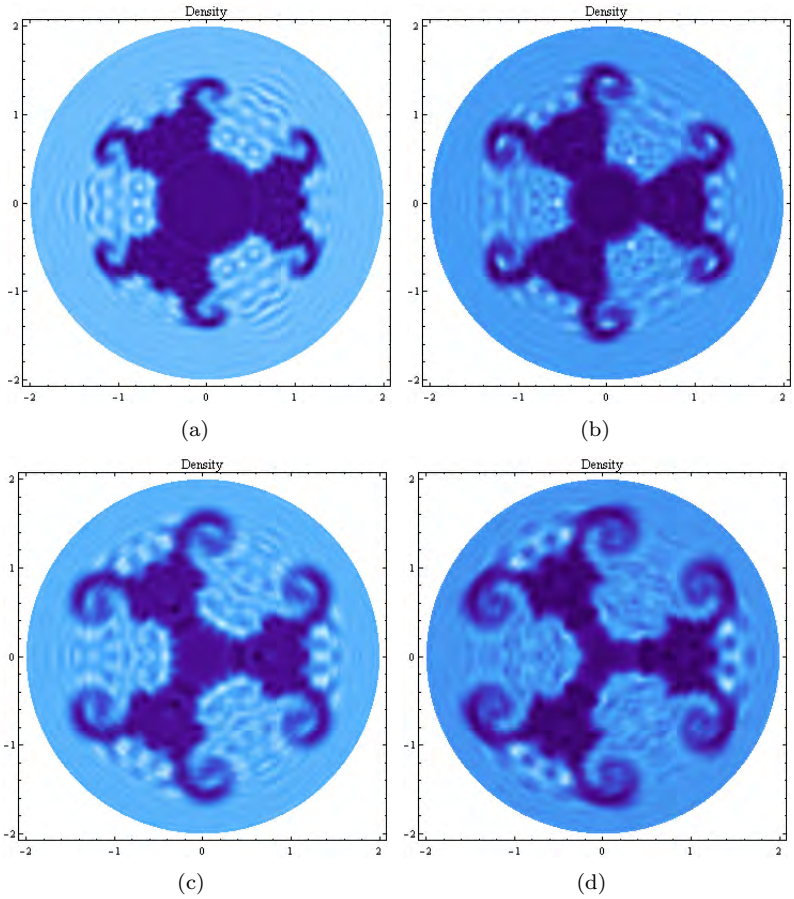

Figure 4.13: Density plot at the four times (a) $t = 6$, (b) $t = 9$, (c) $t = 12$ and (d) $t = 15$ in the absence of a magnetic field, showing the lighter fluid in purple (dark), and the heavier fluid in blue (soft). The magnetic Froude number is $G = 8$ and the disturbance mode is $K = 3$.

configuration of the two fluids was observed as the magnetic Reynolds number varied. The main observation is that, in contrast to Cartesian geometry where the magnetic field had a universal stabilising effect on the flow, in cylindrical geometry, the magnetic field stabilised some parts of the flow, but de-stabilised others. This non-universal behaviour has been observed many times in the literature [33], but is normally associated with certain modes being stable whilst others are unstable. It is conjectured that it is the injection of fluid that is responsible for the behaviour observed in the present chapter.

This chapter considered the MRTI in cylindrical coordinates, which whilst

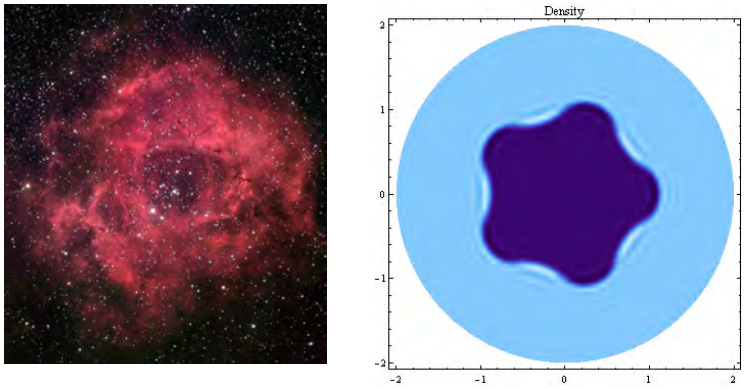

(a) (b)

Figure 4.14: The Rosette nebula (Credit: Robert Gendler [46]) and a density plot at time $t = 1$, showing the lighter fluid in purple (dark), and the heavier fluid in blue (soft). The magnetic Froude number is $G = 1$ and the disturbance mode is $K = 5$.

being a well known problem, has not been studied in the case where there are dipole type singularities at the origin. The dipole type singularities were chosen over, say, a source type singularity due to the impossibility of such a singularity in the magnetic case in view of the divergence-free nature of any magnetic field. The disturbances considered focussed mainly on those that were expected to produce bi-polar plumes, such as those observed by astrophysicists in jet structures, pictures of which may be found in [54]. The flows observed in this chapter did not form the typical thin jet structures even in the case of large magnetic fields. An obvious extension of the bipolar results is to consider higher modes, with different numbers of outflow plumes. This has been illustrated in this chapter for the tripolar case $K = 3$. In addition, more complex multi-mode initial disturbances might also be investigated. Other geometries are also possible, such as cylindrical coordinates with radial or azimuthal symmetry, or various 2D spherical coordinate systems, or indeed some more general 3D geometry. In the latter case, the stream function technique would not be so straightforward,

and it is expected that some sort of constrained transport method would be required to keep the magnetic field divergence free.

The results from this chapter are able to be partially verified by real observations in the field of astrophysics, in particular HII regions and nebulae. Many examples were found that exhibited the same striking features as obtained by the simulated results using the methodology developed in this chapter. In particular, the hourglass, butterfly, tarantula and Rosette nebulae are examples that exhibit a wide range of behaviours over a wide range of parameters, such as the magnetic Froude number.

Chapter 5

Conclusion

This thesis considered three different scenarios of the magnetic Rayleigh-Taylor instability. The consideration of accuracy, efficiency and stability of the solution ultimately dictated that different solution techniques were required to be implemented for each scenario. This is particularly evident in the difference between the model of chapter two with that of chapters three and four. The linear model of chapter two allows a very life like representation of the system as two distinct fluids with an infinitely thin interface located in between. This simpler model is still accurate provided that the assumptions under which it is valid are understood. The models of chapters three and four are valid under more general conditions, and as such are more complicated, for example by the inclusion of weak compressibility and viscosity. The efficiency and stability of the solution in these cases dictates that such a life like representation of the fluids be replaced with an approximation of just a single fluid in which the density varies very rapidly yet smoothly in the region simulating an interface. The models themselves were chosen with a view to being applicable to situations such as HII regions and nebulae from the field of astrophysics. As such, a full treatment modelling every quantity is unnecessary; for example, arguments are presented justifying the fact that temperature considerations are ignored.

The linear model presented in the introductory second chapter considers the

MRTI in Cartesian geometry under the assumption that the amplitude of the disturbing waves is small compared to the wavelength. The advantage of the simpler linear model is that exact analytic solutions are obtained. The model is valid at early time periods, but due to the exponential growth rate that is calculated for the amplitude of such waves at the interface, there will inevitably become such a time in which the assumptions of the model are violated and the results thereafter are meaningless. The growth rate of the interface is obtained for the cases in which the base magnetic field is horizontal, vertical and indeed at any angle by use of superposition. These rates agree with earlier work by Chandrasekhar [13] despite the different approach taken by that author. The rates also agree in the limit of no magnetic field with the well known Atwood number from the pioneering works of Rayleigh [50] and Taylor [59]. The purpose of calculating the growth rates analytically in the linear regime is so that the growth rates for non-linear models obtained by numerical methods in chapter three can be verified to be accurate at least for early time periods where the approximations used in the linear model are valid.

Chapter three builds on the work from chapter two by adding additional non-linear effects to the model, such as convective acceleration, weak compressibility, viscosity and finite conductivity. The more complicated non-linear model requires some type of numerical method since analytic solutions are not available. Common finite difference numerical methods not only require a great amount of computational resources, but also suffer from instability. In addition, such methods can not solve a key equation of the model exactly, the equation specifying that the magnetic field must have zero divergence. We can improve the accuracy, efficiency and stability of the solution by performing a combination of analytic and numerical techniques with a so called pseudo spectral method. The numerical component of this technique uses a tri-diagonal matrix method which is very fast compared with a full finite difference scheme. This has the added bonus that the analytic component of the technique that uses vorticity and streamfunction methods is crucial to be being able to understand and ex-

plain the behaviour of the flow. Various mushroom type shapes are obtained for the interface between the two fluids. Of particular interest is the mechanism for which the magnetic field suppresses the growth of such shapes, for both single mode and multi mode disturbances, and for base magnetic fields directed at various angles. It is also shown that the presence of a magnetic field can prevent bubbles of fluid breaking apart as is observed in the non-magnetic case.

The final scenario is considered in chapter four and adds the complication of circularly symmetric cylindrical geometry. The convergent nature of such geometry is dealt with by the use of dipole type singularities at the origin for both fluid flow and magnetic field. This is typically expected to apply to the cases of HII regions, nebulae and astrophysical jets. In keeping with the considerations of accuracy, efficiency and stability, the numerical method chosen for this chapter differs slightly from that used in the previous chapter. Double series techniques are used in the present case, not only to, satisfy the dipole nature of the flows at the origin exactly, but also to maintain the divergence-free nature of the magnetic field exactly while allowing the very efficient Runge-Kutta RK4 method to be used to integrate the system of PDEs forwards in time. Of interest is how the flow evolves into an integer number of plumes dependent on the integer wave number of the disturbing wave. The shapes obtained bear striking similarity to those observed in real HII regions and nebulae, which are topics of frontier research in astrophysics.

The work of this thesis has scope for various extensions. Additional effects such as surface tension would be compatible with the methods of either chapters three or four. It would also be straightforward to apply the methods to cylindrical geometry with radial or azimuthal symmetry or two dimensional spherical geometry, each of which would have applications in astrophysics. Less straightforward but still possible would be to consider three dimensional versions of the instability. The greatest difficulty for the three dimensional version would be the maintenance of the divergence free nature of the magnetic field. It is expected that some type of constrained transport algorithm would be required in

such a case. It is not known whether the inclusion of relativistic effects would be compatible with the methods used in this thesis, and would require further research. Even within the current model of chapter four, there is scope for further work by considering different types of disturbances, in particular multi-mode disturbances. In chapter three it was shown that there is a vast difference in behaviour between the single mode and multi-mode disturbances, and the same may be possible for the conditions of chapter four.

Bibliography

[1] M. Abramowitz and I.A. Stegun. *Handbook of Mathematical Functions*. Dover Publications Inc., New York, USA, 10th edition, 1972.

[2] W. Ames. *Numerical Methods for Partial Differential Equations*. Academic Press, New York, 1977.

[3] J. Anderson and M. Watzke. Tarantula nebula. http://www.nasa.gov/mission_pages/chandra/multimedia/tarantula2012.html, 2012.

[4] S. Arthur, W. Henney, G. Mellema, F. De Colle, and E. Vázquez-Semadeni. Radiation-magnetohydrodynamic simulations of HII regions and their associated PDRs in turbulent molecular clouds. *MNRAS*, 414:1747–1768, 2011.

[5] K. Atkinson. *An Introduction To Numerical Analysis*. John Wiley and Sons Inc., New York, 1978.

[6] G. Batchelor. *An Introduction to Fluid Dynamics*. Cambridge University Press, Cambridge, 1967.

[7] M. Bate, I. Bonnell, and N. Price. Modelling accretion in protobinary systems. *MNRAS*, 277:362–376, 1995.

[8] G.I. Bell. Taylor instability on cylinders and spheres in the small amplitude approximation. Report LA-1321, Los Alamos Laboratory, 1951.

[9] J.U. Brackbill and D.C. Barnes. The Effect of Nonzero $\nabla \cdot \boldsymbol{B}$ on the Numerical Solution of the Magnetohydrodynamic Equations. *Journal of Computational Physics*, 35:426–430, 1980.

[10] J. Cao, H. Ren, Z. Wu, and P. Chu. Quantum effects on Rayleigh-Taylor instability in magnetised plasma. *Physics of Plasmas*, 15, 2008.

[11] K. Chambers and L.K. Forbes. The magnetic Rayleigh-Taylor instability for inviscid and viscous fluids. *Physics of Plasmas*, 18, 2011.

[12] K. Chambers and L.K. Forbes. The cylindrical magnetic Rayleigh-Taylor instability for viscous fluids. *Physics of Plasmas*, 2012.

[13] S. Chandrasekhar. *Hydrodynamic and Hydromagnetic Stability.* Dover Publications Inc., New York, 1981.

[14] M. Chen and L. Forbes. Accurate methods for computing inviscid and viscous Kelvin-Helmholtz instability. *Journal of Computational Physics*, 230:1499–1515, 2011.

[15] P. Colella and P. Woodward. The piecewise parabolic method (ppm) for gas dynamic simulations. *Journal of Computational Physics*, 54:174–201, 1984.

[16] R. Crutcher. Magnetic fields in molecular clouds: observations confront theory. *The Astrophysical Journal*, 520:706–713, 1999.

[17] J. Dale and I. Bonnell. The effect of stellar winds on the formation of a protocluster. *MNRAS*, 391:2–13, 2008.

[18] J. Dale and I. Bonnell. Ionizing feedback from massive stars in massive clusters: Fake bubbles and untriggered star formation. *The Astrophysical Journal*, 414:321–328, 2011.

[19] P. Davidson. *An Introduction to Magnetohydrodynamics.* Cambridge University Press, 2001.

[20] R. Epstein. On the Bell-Plesset effects: The effects of uniform compression and geometrical convergence on the classical Rayleigh-Taylor instability. *Physics of Plasmas*, 11, 2004.

[21] ESA, NASA, ESO, and D. LaCrue. In the heart of the tarantula nebula. http://apod.nasa.gov/apod/ap090331.html, 2009.

[22] ESO ESA, NASA and D.LaCrue. In the heart of the tarantula nebula. http://apod.nasa.gov/apod/ap090331.html, 2009.

[23] D.E. Farrow and G.C. Hocking. A numerical model for withdrawal from a two-layer fluid. *J Fluid Mech.*, 549:141–157, 2006.

[24] L.K. Forbes. The Rayleigh-Taylor instability for inviscid and viscous fluids. *J Eng Math*, 65:273–290, 2009.

[25] L.K. Forbes. A cylindrical Rayleigh-Taylor instability: radial outflow from pipes or stars. *J Eng Math*, 70:205–224, 2011.

[26] N. Fukuda and T. Hanawa. Sequential star formation triggered by expansion of an HII region. *The Astrophysical Journal*, 533:911–923, 2000.

[27] L. Gendelev and M. Krumholz. Evolution of blister-type HII regions in a magnetized medium. *The Astrophysical Journal*, 745:158, 2012.

[28] E.G. Harris. Rayleigh-Taylor instabilities of a collapsing cylindrical shell in a magnetic field. *Physics of Fluids*, 5, 1962.

[29] H. Helmholtz. *Über discontinuierliche Flüssigkeitsbewegungen.* Monatsberichte der Königlichen Akademie der Wissenschaften, Berlin, 1868.

[30] W. Henney, S. Arthur, F. De Colle, and G. Mellema. Radiation-magnetohydrodynamic simulations of the photoionization of magnetized globules. *MNRAS*, 398:157–175, 2009.

[31] J.D. Hoffman. *Numerical Methods for Engineers and Scientists.* Marcel Dekker, Inc., New York, 2001.

[32] H. Isobe, T. Miyagoshi, K. Shibata, and T. Yokoyama. Three dimensional simulation of solar emerging flux using the earth simulator I. Magnetic Rayleigh-Taylor instability at the top of the emerging flux as the origin of filamentary structure. *Publ. Astron. Soc. Japan*, 58:423–438, 2006.

[33] B. Jun, M. Norman, and J. Stone. A numerical study of Rayleigh-Taylor instability in magnetic fluids. *The Astrophysical Journal*, 453:332–349, 1995.

[34] F. Kahn. The acceleration of interstellar clouds. *B.A.N.*, 12:187–200, 1954.

[35] Lord Kelvin. *Mathematical and Physical Papers.* Cambridge University Press, England, 1910.

[36] E. Kreyszig. *Advanced Engineering Mathematics.* John Wiley and Sons Inc., 8th edition, 1999.

[37] A. Kurosh. *Higher Algebra.* Mir Publishers, Moscow, 2nd edition, 1975.

[38] R. Matsumoto. Network laboratory system for space simulations. http://www.rish.kyoto.u.ac.jp/isss7/CDROM/CONTENTS/DATA_PDF/T-RMAT.PDF, 2005.

[39] C. Matsuoka and K. Nishihara. Analytical and numerical study on a vortex sheet in incompressible Richtmyer-Meshkov instability in cylindrical geometry. *Phys. Rev. E*, 74:066303, 2006.

[40] C. Matsuoka and K. Nishihara. Fully nonlinear evolution of a cylindrical vortex sheet in incompressible Richtmyer-Meshkov instability. *Phys. Rev. E*, 73:055304, 2006.

[41] E.E. Meshkov. Instability of the interface of two gases accelerated by a shock wave. *Izv. AN SSSR Mekhanika Zhidkosti i Gaza*, 4:151–157, 1969.

[42] L. Mestel and L. Spitzer, Jr. Star formation in magnetic dust clouds. *MNRAS*, 116:503–514, 1956.

[43] K.O. Mikaelian. Rayleigh-Taylor and Richtmyer-Meshkov instabilities and mixing in stratified cylindrical shells. *Physics of Fluids*, 17, 2005.

[44] A. Mizuta, J. Kane, M. Pound, B. Remington, D. Ryutov, and H.Takabe. Hydrodynamic instability of ionization fronts in HII regions. *The Astrophysical Journal*, 621:803–807, 2005.

[45] NASA, ESA, and The Hubble SM4 ERO Team. NGC 6302. http://www.nasa.gov/mission_pages/hubble/multimedia/ero/ero_ngc6302.html, 2009.

[46] R. Nemiroff and J. Bonnell. The Rosette nebula. http://apod.nasa.gov/apod/ap010214.html, 2001.

[47] G. Pacitto, C. Flament, J.-C. Bacri, and M. Widom. Rayleigh-Taylor instability with magnetic fluids: Experiment and Theory. *The American Physical Society*, 62:7941–7948, 2000.

[48] E.N. Parker. The dynamical state of the interstellar gas and field. *Journal of Astrophysics*, 145:811, 1966.

[49] M.S. Plesset. On the stability of fluid flows with spherical symmetry. *J Appl. Phys.*, 25, 1954.

[50] Lord Rayleigh. Investigation of the character of the equilibrium of an incompressible heavy fluid of variable density. *London Math Society*, 14:170–177, 1883.

[51] R.D. Richtmyer. Taylor instability in shock acceleration of compressible fluids. *Communications on Pure and Applied Mathematics*, 13, 1960.

[52] R. Sahai, J. Trauger, The WFPC2 Science Team, and NASA. Hubble finds an hourglass nebula around a dying star. http://hubblesite.org/newscenter/archive/releases/1996/07/, 1996.

[53] L. Spitzer, Jr. *Physical processes in the interstellar medium.* Wiley Inc., New York, 1978.

[54] S. Stahler and F. Palla. *The formation of stars*. Wiley-VCH, Berlin, 2004.

[55] J. Stone. The ZEUS code for astrophysical magnetohydrodynamics: new extensions and applications. *Journal of Computational and Applied Mathematics*, 109:261–280, 1999.

[56] J. Stone, T. Gardiner, P. Teuben, J. Hawley, and J. Simon. Athena: A new code for astrophysical MHD. *The Astrophysical Journal Supplement Series*, 178:137–177, 2008.

[57] J.M. Stone and T. Gardiner. Non-linear evolution of the magnetohydrodynamic Rayleigh-Taylor instability. *Physics of Fluids*, 19, 2007.

[58] B. Strömgren. The physical state of interstellar hydrogen. *The Astrophysical Journal*, 89:526–547, 1939.

[59] Sir G.I. Taylor. The instability of liquid surfaces when accelerated in a direction perpendicular to their planes. *I. Proc R Soc*, 201:192–196, 1950.

[60] B. van Leer. Towards the ultimate conservative difference scheme. *Journal of Computational Physics*, 32:101–136, 1979.

[61] G. von Winckel. lgwt.m. http://www.mathworks.com/matlabcentral/ fileexchange/loadFile.do?objectId=4540&objectType=file, 2004.

[62] R. Williams. Shadowing instabilities of ionization fronts. *MNRAS*, 310:789–796, 1999.

[63] H. Yu and D. Livescu. Rayleigh-Taylor instability in cylindrical geometry with compressible fluids. *Physics of Fluids*, 20, 2008.

[64] W. Zhang, Z. Wu, and D. Li. Effect of shear flow and magnetic field on the Rayleigh-Taylor instability. *Physics of Plasmas*, 12, 2005.